International Journal of Pharmaceutics 664 (2024) 124635

Contents lists available at ScienceDirect

International Journal of Pharmaceutics

journal homepage: www.elsevier.com/locate/ijpharm

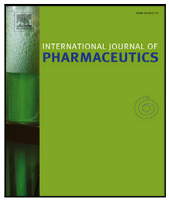

A two-stage mechanistic reduced-order model of pharmaceutical tablet dissolution: Population balance modeling and tablet wetting functions

Shumaiya Ferdoush [a], Marcial Gonzalez [a,b,*]

[a] School of Mechanical Engineering, Purdue University, West Lafayette, IN 47907, USA
[b] Ray W. Herrick Laboratories, Purdue University, West Lafayette, IN 47907, USA

ARTICLE INFO

Keywords:
Two-stage mechanistic model
Population balance model
Tablet wetting function
Tablet dissolution
Tablet porosity
Crystal size distribution

ABSTRACT

We propose a two-stage reduced-order model (ROM) of pharmaceutical tablet dissolution that is comprised of (i) a mechanistic dissolution function of the active pharmaceutical ingredient (API) and (ii) a tablet wetting function. The former is derived from a population balance model, using a high-resolution finite volume algorithm for a given API crystal size distribution and dissolution rate coefficient. The latter is obtained from the mechanistic understanding of water penetration inside a porous tablet, and it estimates the rate at which the API is exposed to the buffer solution for a given formulation and the dimensions of the tablet, contact angle, and surface tension between the solid and liquid phases, liquid viscosity, and mean effective capillary radius of the pore solid structure. In turn, the two-stage model is mechanistic in nature and one-way coupled by means of convolution in time to capture the start time of the API dissolution process as water uptake, swelling, and disintegration take place. The two-stage model correlates dissolution profiles with critical process parameters (CPPs), critical material attributes (CMAs), and other crucial critical quality attributes (CQAs). We demonstrate the model's versatility and effectiveness in predicting the dissolution profiles of diverse pharmaceutical formulations. Specifically, we formulate and fabricate acetaminophen and lomustine solid tablets using different API content and size distributions, characterize their dissolution behavior, and estimate capillary radius as a function of tablet porosity. The estimations generated by the proposed models consistently match the experimental data across all cases investigated in this study.

1. Introduction

The U.S. Food and Drug Administration's (FDA) guidelines for implementing Quality by Design (QbD) in the pharmaceutical manufacturing process emphasize using systematic approaches to process development, incorporating a deeper understanding of both process and product rooted in robust scientific principles (FDA and CDER, 2006). The identification of critical quality attributes (CQAs) of pharmaceutical products allows for the use of mechanistic and mathematical models to understand how critical material attributes (CMAs) and critical process parameters (CPPs) influence CQAs. With the help of this information, one can find out the design space (DS), within which the process can function without compromising the target product profile (TPP) despite changes in operating conditions (Lawrence et al., 2014). Expanding the QbD framework to a Quality by Control (QbC) framework entails integrating active process control strategies (Su et al., 2019). These strategies aim to tackle real-time operational challenges stemming from process disturbances and uncertainties. A pivotal component of this transition involves the development of mechanistic and semi-mechanistic reduced-order models (ROMs). These models are instrumental in facilitating process design, optimization, and control within the realm of pharmaceutical manufacturing (Ferdoush and Gonzalez, 2023).

The dissolution profile emerges as a pivotal CQA for any solid oral dosage form (Lawrence et al., 2014), and it plays a crucial role in determining the bioavailability and therapeutic effectiveness of the pharmaceutical product. One can also use it as a quality control (QC) test and in lieu of bioequivalence testing (Parvaresh et al., 2024). Understanding and controlling the dissolution profile is essential in ensuring consistent and reproducible performance of the solid dosage form. Dissolution tests are time-consuming destructive tests performed offline to ensure product quality (FDA and CDER, 1997). Therefore, predictive dissolution models play a pivotal role in successfully implementing any real-time release testing (RTRT) strategy (FDA, 2004, 2012; Wu et al., 2015).

Describing drug release mechanisms from a pharmaceutical system involves navigating through various complex physical and chemical

* Corresponding author at: School of Mechanical Engineering, Purdue University, West Lafayette, IN 47907, USA.
E-mail address: marcial-gonzalez@purdue.edu (M. Gonzalez).

https://doi.org/10.1016/j.ijpharm.2024.124635
Received 13 April 2024; Received in revised form 24 July 2024; Accepted 22 August 2024
Available online 24 August 2024

phenomena (Costa and Lobo, 2001). When combined with precise experimental observations, models that capture mechanistic theories help gain a deeper understanding of the drug release mechanism (Peppas and Narasimhan, 2014). Zaborenko et al. (2019) discussed the importance of using first-principles models in the early stages of research and development, especially when there is limited data and process understanding. These models can offer guidance for formulation and process development. As more data is generated and a better understanding is gained, a combination of first-principles-based and data-driven empirical approaches becomes feasible. This combined approach helps link CMAs and CPPs to the drug product dissolution profile, ultimately enabling the creation of a predictive dissolution model for batch or real-time release (Zaborenko et al., 2019).

First-principles models, such as population balance models (PBM), have been extensively used for modeling crystallization processes (LeBlanc and Fogler, 1987; Rawlings et al., 1992; Puel et al., 2003; Costa et al., 2007; Lima et al., 2023). However, the PBM has seldom been used to predict *in-vitro* dissolution of a pharmaceutical ingredient (see, e.g., Nagy et al. (2021) and Mangin et al. (2006)). Wilson et al. (2012) studied disintegration and dissolution phenomena for an immediate-release tablet formulation using a dynamic optical particle imaging approach to monitor the number and size of particles entering the dissolution media, coupled with a population balance model. Su et al. (2023) developed a predictive mechanistic dissolution model that consisted of diffusion, dissolution, and population balance of the active pharmaceutical ingredient (API) for tablets, and erosion and swelling of the polymer matrix mainly controlled dissolution. The authors assumed that the tablet size gradually diminishes as a result of matrix erosion, accompanied by the immediate release and dissolution of API particles. However, they have not studied tablets which dissolve by disintegration instead of erosion. Therefore, a predictive tablet dissolution model that is versatile enough to capture dissolution profiles of tablets that dissolve by any physical mechanism is needed. In this work, we propose a mechanistic ROM to predict the dissolution of pharmaceutical tablets that is comprised of (i) a mechanistic API dissolution function $\mathcal{M}_{\text{API}}(t)$ derived from a PBM using a high-resolution finite volume algorithm (HR-FVM) (Nagy et al., 2021; Gunawan et al., 2004) for given API crystal size distribution and dissolution rate coefficient, and (ii) a tablet wetting function $\mathcal{W}_{\text{API}}(t)$ that estimates the rate at which the API is exposed to the buffer solution for given formulation and dimensions of the tablet, contact angle and surface tension between the liquid and solid phases, liquid viscosity, and mean effective capillary radius of the porous solid microstructure (Ferdoush et al., 2023). The two-stage model is mechanistic in nature and one-way coupled by means of convolution in time to capture the start time of the API dissolution process as water uptake, swelling, and disintegration take place. It is interesting to note that the dissolution ROM is a function of CMAs, tablet formulation, and dimensions, which can be estimated from tableting ROMs, CPPs, and other CQAs (e.g., in-process changes in tablet porosity and API content can be estimated from changes in compaction force, and in tablet dimensions and tensile strength Bachawala and Gonzalez, 2022; Bachawala et al., 2024; Su et al., 2018; Huang et al., 2021).

The paper is organized as follows. In Section 2, the mechanistic API dissolution model that solves a PBM using a high-resolution finite volume algorithm (HR-FVM) is discussed. Next, in Section 3, the derivation of a tablet wetting function, which estimates the rate at which the API is exposed to the buffer solution, is presented. In Section 4, the two-stage tablet dissolution ROM, comprised of a mechanistic API dissolution model and a tablet wetting function, is presented. A parameter estimation method is introduced in the same section, aiming to maximize the similarity factor values between model predictions and experimental dissolution data. In Section 5, API dissolution model parameters are estimated using acetaminophen (a pain and fever reliever) and lomustine (an oral medication for treating primary and metastatic brain tumors) crystals' dissolution data. The API dissolution model is next used to predict the in-batch dissolution variability of lomustine dosages. Lastly, wetting function model parameters of the two-stage mechanistic tablet dissolution ROM are estimated using acetaminophen and lomustine tablets' dissolution data. Concluding remarks are detailed in Section 6.

2. Mechanistic API dissolution model

In this section, a population balance model will be used to predict the *in-vitro* dissolution of API crystals. In the U.S. Pharmacopeia (USP) standard apparatus for performing dissolution test (USP, 2011), it is presumed that the time evolution of the population density function $n(L,t)$, denoting the number-based crystal size distribution (CSD), is solely impacted by the dissolution of the particles (Nagy et al., 2021). Therefore, the population balance equation takes the form of

$$\frac{\partial n(L,t)}{\partial t} - \frac{\partial D(L) n(L,t)}{\partial L} = 0 \tag{1}$$

where D is the dissolution rate, t is time, and L is the characteristic size of crystal. The population density function $n(L,t)$ is expressed in terms of the normalized CSD $n_{\text{m}}(L,t)$ as follows (Nagy et al., 2021)

$$n(L,t) = n_{\text{m}}(L,t)\frac{\nu_c}{\mu_3 k_v} \tag{2}$$

where k_v is the volumetric shape factor defined as the ratio of the volume of a particle (spherical) and a cube with sides equal to the particle diameter, and ν_c is the proportion of the sample volume within the dissolution medium at $t = 0$, i.e.,

$$\nu_c = \frac{m_{\text{API}}/\rho_{\text{API}}}{m_{\text{API}}/\rho_{\text{API}} + V_{\text{D}}} \tag{3}$$

with m_{API} being the total mass of the API, ρ_{API} the density of the API, and V_{D} the dissolution media volume. μ_3 is the third moment of the distribution given by

$$\mu_3 = \int_0^\infty L^3 n_{\text{m}}(L,0)\,\text{d}L \tag{4}$$

Using Eq. (2), Eq. (1) is rewritten as

$$\frac{\partial n_{\text{m}}(L,t)}{\partial t} - \frac{\partial D(L) n_{\text{m}}(L,t)}{\partial L} = 0 \tag{5}$$

with boundary conditions given by

$$n_{\text{m}}(L \to \infty, t) = 0$$

The rate of dissolution is size-dependent, in general, and defined as

$$D(L) = k_{\text{API}}\,\sigma_{\text{d}}^{d}(1 + p_1 L)^{p_2} \tag{6}$$

where k_{API} represents the dissolution rate coefficient, d signifies the exponent of the dissolution rate, σ_{d} denotes the relative supersaturation, and p_1 and p_2 are size dependent dissolution coefficients. Since a low amount of solid is dissolved in the USP apparatus relative to the solvent volume, sink conditions are attained, and supersaturation is irrelevant. Nagy et al. (2011) used this model for studying potassium alum dissolution in water, with $k_{\text{API}} = 1.28$ μm/s, $d = 0.98$, $p_1 = 0.02/\mu\text{m}$, and $p_2 = 0.86$. However, in this work, for simplicity and as it has been assumed by Nagy et al. (2021) for dissolution of acetylsalicylic acid (ASA), crystal size dependency is neglected and, thus, $D = k_{\text{API}}$. It is worth mentioning that Litster (2016) presented a different expression of the size-dependent dissolution rate, where the dissolution rate varies inversely with respect to the crystal size, by assuming that particles travel with streamlines inside the vessel and the solution is very dilute (i.e., stagnant condition and a small Sherwood number of 2).

The rate of change of API mass dissolved in a volume of total solution equal to $V_{\text{L}}(t)$, such that $V_{\text{D}} \le V_{\text{L}}(t) \le m_{\text{API}}/\rho_{\text{API}} + V_{\text{D}}$, is given by

$$\frac{d M_{\text{API}}(t)}{dt} = V_{\text{L}}(t)\left[3\rho_{\text{API}} k_v k_{\text{API}} \int_0^\infty L^2 n(L,t)\text{d}L\right] \tag{7}$$

where the second moment of distribution is used to determine the total crystal surface area and the rate of change of concentration of the solute in the solution (see, e.g., Ranodolph (2012) and Rawlings et al. (1993)). As noted above, inside the USP apparatus $V_{\text{D}} \approx V_{\text{L}}$ and, in turn, the total mass of API in the dissolution media at time t is given by

$$M_{\text{API}}(t) = 3 m_{\text{API}} k_{\text{API}} \int_0^t \int_0^\infty \frac{1}{\mu_3} L^2 n_{\text{m}}(L,\tau)\,d\,L\,d\,\tau \tag{8}$$

with $M_{\mathrm{API}}(0) = 0$ (Nagy et al., 2021). The fraction of drug released is then expressed as

$$\mathcal{M}_{\mathrm{API}}(t) = \frac{M_{\mathrm{API}}(t)}{m_{\mathrm{API}}} = 3k_{\mathrm{API}} \int_0^t \int_0^\infty \frac{1}{\mu_3} L^2 n_{\mathrm{m}}(L,\tau)\, dL\, d\tau \tag{9}$$

and is determined by using a high-resolution finite volume algorithm (HR-FVM) to solve the balance equation, as discussed next in turn.

2.1. High-resolution finite volume algorithm (HR-FVM)

A high-resolution finite volume method was employed to solve the population balance Eq. (5). The high-resolution finite volume algorithm with second order accuracy is written as follows (Gunawan et al., 2004)

$$n_{m,i}^{k+1} = n_{m,i}^{k} + \frac{\Delta t\ k_{\mathrm{API}}}{\Delta x}(n_{m,i+1}^{k} - n_{m,i}^{k}) - \frac{\Delta t\ k_{\mathrm{API}}}{2\Delta x}\left(1 - \frac{\Delta t\ k_{\mathrm{API}}}{\Delta x}\right)\left[(n_{m,i+1}^{k} - n_{m,i}^{k})\phi_{i+1} - (n_{m,i}^{k} - n_{m,i-1}^{k})\phi_i\right] \tag{10}$$

where k is used for time discretization, i is used for spatial discretization, Δt is the time step, and Δx is the size step. The flux limiter function $\phi_i = \phi(\theta_i)$ is evaluated based on the ratio of two consecutive gradients and is dependent on the distribution's smoothness level

$$\theta_i = \frac{(n_{m,i+1}^{k} - n_{m,i}^{k}) + \epsilon}{(n_{m,i}^{k} - n_{m,i-1}^{k}) + \epsilon} \tag{11}$$

The Van Leer flux limiter provides full second-order accuracy (Van Leer, 1974) and is expressed as

$$\phi(\theta_i) = \frac{|\theta_i| + \theta_i}{1 + |\theta_i|} \tag{12}$$

In the case of one-dimensional problems, this approach exhibits total variation diminishment, ensuring that the algorithm avoids introducing numerical dispersion. The discrete version of the fraction of API released is then given by

$$\mathcal{M}_{\mathrm{API}}^{k+1} = \mathcal{M}_{\mathrm{API}}^{k} + \frac{3k_{\mathrm{API}}}{\mu_3}\ \Delta t \sum_i L_i^2 n_{\mathrm{m}}(L_i, t_k)\Delta L \tag{13}$$

with $\mathcal{M}_{\mathrm{API}}^{0} = 0$.

3. Tablet wetting functions

This section will first present a one-dimensional tablet wetting function determined experimentally from axial water penetration inside a pharmaceutical acetaminophen tablet using time-resolved micro-CT tests carried out by Ferdoush et al. (2023). Inside the USP apparatus, water penetration takes place in a direction perpendicular to the table surface. Therefore, we will derive a three-dimensional tablet wetting function by restricting attention to a flat-faced cylindrical tablet for simplicity and assuming that the liquid penetration rate is equal in both axial and radial directions.

3.1. One dimensional tablet wetting function

Ferdoush et al. (2023) studied axial water penetration (see Fig. 1) inside a flat-faced cylindrical pharmaceutical tablet using a time-resolved micro-CT test. The tablet formulation comprised of 89% microcrystalline cellulose (MCC, Avicel PH 200), 9% acetaminophen (APAP), 1% magnesium stearate (MgSt), and 1% colloidal silica dioxide (Cab-O-Sil), all % w/w. APAP was obtained from Mallinckrodt Pharmaceuticals, US, MCC was obtained from DuPont Nutrition, US, MgSt was obtained from Spectrum Chemical Mfg. Corp., New Brunswick, NJ, US, and Cab-O-Sil was obtained from Cabot Corporation, IL, US. The authors studied that the amount of water inside a tablet depends on the

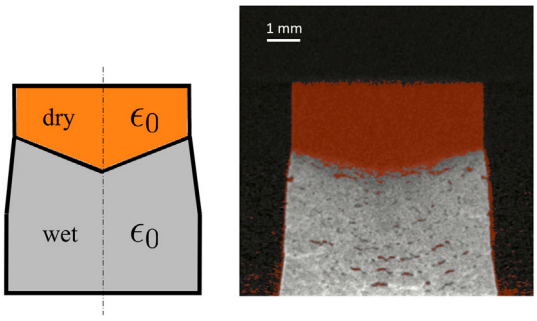

Fig. 1. Water penetration from the bottom inside a flat-faced cylindrical tablet, pictures obtained from Ferdoush et al. (2023). The color orange indicates the dry tablet, while gray signifies the tablet in its wet and swollen state. The liquid front is the interface between dry (orange) and wet (gray).

tablet's relative density or porosity. The integration of liquid penetration driven by capillary pressure, as elucidated by the Lucas–Washburn theory (Hamraoui and Nylander, 2002), with the swelling kinetics of the excipients following a first-order process (Schott, 1992a,b), enabled the provision of a physical interpretation for the experimental observations concerning water absorption by both the excipients and the porous space within the tablet. The author noted that the water absorbed by the excipients is expressed as

$$V_{\mathrm{water}}^{\mathrm{exc}}(t) = \underbrace{\pi R_{\mathrm{tab}}^2 \sqrt{\frac{r_e \gamma \cos\theta}{2\eta}} \int_0^\tau \frac{(1-\epsilon_0)}{2\sqrt{\hat{t}}}}_{\text{wet solid: capillary intake}} \left[x_{\mathrm{exc}}\, \underbrace{\mathrm{WAC}\frac{\rho_{\mathrm{true}}}{\rho_{\mathrm{H_2O}}}\left(1 - \mathrm{e}^{-k(t-\hat{t})}\right)}_{\text{swelling kinetics}} \right] \mathrm{d}\hat{t}$$
$$= (1-\epsilon_0)\pi R_{\mathrm{tab}}^2 \sqrt{\frac{r_e \gamma \cos\theta\ \tau}{2\eta}}\, x_{\mathrm{exc}} \mathrm{WAC}\frac{\rho_{\mathrm{true}}}{\rho_{\mathrm{H_2O}}}\left(1 - \frac{F(\sqrt{k\tau})}{\sqrt{k\tau}}\mathrm{e}^{-k(t-\tau)}\right)$$
$$\text{with}\quad \tau = \min[t, 2H_{\mathrm{tab}}^2 \eta / r_e \gamma \cos\theta] \tag{14}$$

where R_{tab} is the dry radius of the tablet, r_e represents the mean effective capillary radius of the porous microstructure, γ and η represent the surface tension and viscosity of the liquid, respectively, θ denotes the contact angle between solid and liquid, $F(\cdot)$ is the Dawson integral, $2H_{\mathrm{tab}}^2\eta/r_e\gamma\cos\theta$ is the time at which the wet front reaches the upper surface of the tablet, x_{exc} is defined as the concentration (w/w) of the excipients experiencing swelling, and H_{tab} is the height of the dry tablet. In the equation shown above, ρ_{true} stands for the true density of the powder blend, $\rho_{\mathrm{H_2O}}$ denotes the density of water, WAC represents the water-retention capacity of the excipients (Witono et al., 2014), and k signifies the swelling rate constant governing the first order swelling kinetics (Schott, 1992a,b). The above equation implies that the swellable excipients will undergo equilibrium swelling behind the liquid front, as shown in Fig. 1. The liquid front advances faster in tablets with low relative density (or high porosity) than in tablets with high relative density (or low porosity) (Ferdoush et al., 2023). The water contained within the porous space is then expressed as

$$V_{\mathrm{water}}^{\mathrm{void}}(t) = \underbrace{\epsilon_0\, \pi R_{\mathrm{tab}}^2 \sqrt{\frac{r_e \gamma \cos\theta\ \tau}{2\eta}} \left[1 + \underbrace{x_{\mathrm{exc}}\, \mathrm{WAC}\frac{\rho_{\mathrm{true}}}{\rho_{\mathrm{H_2O}}}\left(1 - \frac{F(\sqrt{k\tau})}{\sqrt{k\tau}}\mathrm{e}^{-k(t-\tau)}\right)}_{\text{swollen fraction}} \right]}_{\text{total volume of the tablet after swelling}} \tag{15}$$

Thus, the total volume of water contained within the tablet is written as follows

$$V_{\text{water}}(t) = V^{\text{exc}}_{\text{water}}(t) + V^{\text{void}}_{\text{water}}(t) = \pi R^2_{\text{tab}} \sqrt{\frac{r_e \gamma \cos\theta\ \tau}{2\eta}} \times \left[\epsilon_0 + x_{\text{exc}} \text{WAC} \frac{\rho_{\text{true}}}{\rho_{H_2O}} \left(1 - \frac{F(\sqrt{k\tau})}{\sqrt{k\tau}} e^{-k(t-\tau)}\right)\right] \tag{16}$$

Now, the first portion of Eq. (14) is the volume of the wet solid where liquid penetration occurs as a result of capillary pressure and is obtained from the Washburn equation (Washburn, 1921). The kinetics of the liquid front wetting the tablet are independent of whether there is any swelling inside the tablet, as swelling happens behind the liquid front. We are only interested in the kinetics of the liquid front wetting the entire tablet; thus, we will only work with the Washburn equation, and the second portion of Eq. (14) does not show up in the following expressions. We assume the API mass is uniformly distributed over the entire tablet volume. Thus, the wet API fraction for axial water penetration is equal to the wet volume fraction and is expressed as

$$\mathcal{W}_{\text{API}}(t) = \begin{cases} \frac{1}{H_{\text{tab}}} \sqrt{\frac{r_e \gamma \cos\theta\ t}{2\eta}} & \text{for } t \in [0, \tau) \\ 1 & \text{for } t \in [\tau, \infty) \end{cases} \tag{17}$$

with $\tau = 2H^2_{\text{tab}}\eta / r_e \gamma \cos\theta$. The rate of tablet wetting is expressed as

$$\dot{\mathcal{W}}_{\text{API}}(t) = \begin{cases} \frac{1}{H_{\text{tab}}} \sqrt{\frac{r_e \gamma \cos\theta}{2\eta}} \frac{1}{2\sqrt{t}} & \text{for } t \in [0, \tau) \\ 0 & \text{for } t \in [\tau, \infty) \end{cases} \tag{18}$$

Model parameters such as WAC, k and r_e are estimated by using Eqs. (14) and (15) with respect to the experimental data in Figs. 2(a) and 2(b), respectively. The findings suggest that the amount of water absorbed by the excipients remains unaffected by the tablet's relative density, whereas water absorbed by the porous space depends on the tablet's relative density. The estimated effective capillary radius values for the acetaminophen tablets reported by Ferdoush et al. (2023) are 10 nm, 7.3 nm, 6.9 nm, and 5.5 nm for tablet porosity of 0.26, 0.23, 0.17, and 0.14 respectively. The authors also concluded that intra-particle porosity influences water penetration instead of inter-particle porosity. The estimated effective capillary radius values were used in Eq. (17) to predict the experimental trend of wet API fraction as shown in Fig. 2(c) and Eq. (18) to predict the experimental trend of rate of tablet wetting as shown in Fig. 2(d). The model prediction aligns well with respect to the experimental data points. When the wet API fraction reaches one in Fig. 2(c), the tablet is entirely wet, and the entire amount of API inside the tablet has started dissolving. Similarly, the rate of tablet wetting goes to zero, as shown in Fig. 2(d) when the tablet is entirely wet. The rate of tablet wetting is high at the beginning of the wetting process and then slows down towards the end of wetting.

3.2. Three dimensional tablet wetting function

The expression of wet API fraction shown in Eq. (17) is for water penetration in the axial direction only. However, both axial and radial water penetration happens inside the tablet during tablet dissolution. The well-known Washburn equation illustrates the liquid front height, L, when liquid is introduced from the bottom in a porous medium (Washburn, 1921). Hyväluoma et al. (2006), Danino and Marmur (1994), Borhan and Rungta (1993) and Marmur (1988) studied radial capillary penetration of liquid in between two parallel plates and paper and noted that there is a slight decrease in the rate of radial penetration compared to the axial penetration. For simplicity, we assume that the liquid penetration rate inside the tablet is equal in both axial and radial directions and is expressed as

$$\dot{L} = \dot{R} = \sqrt{\frac{r_e \gamma \cos\theta}{2\eta}} \frac{1}{2\sqrt{t}} \tag{19}$$

It is worth mentioning that the radial and axial liquid front (from top and bottom) will advance simultaneously until one or both of the liquid front reaches the center of the tablet. The radial and/or the axial liquid front will reach the center of the tablet, depending on the tablet's dimension. If the dry diameter of the tablet is larger than the dry height, the axial liquid front will reach the center first (Fig. 3), and vice versa. If the dry radius is equal to the dry height, both the liquid front will reach the center of the tablet at the same time.

Now, the wet volume fraction of the tablet is expressed as follows

$$\overline{V}_{\text{wet}}(t) = \begin{cases} 1 - \left(1 - \frac{R(t)}{R_{\text{tab}}}\right)^2 \left(1 - \frac{2L(t)}{H_{\text{tab}}}\right) & \text{for } t \in [0, \tau) \\ 1 & \text{for } t \in [\tau, \infty) \end{cases} \tag{20}$$

Thus, the wet API fraction is written as

$$\mathcal{W}_{\text{API}}(t) = \begin{cases} 1 - \left(1 - \frac{1}{R_{\text{tab}}} \sqrt{\frac{r_e \gamma \cos\theta\ t}{2\eta}}\right)^2 \left(1 - \frac{2}{H_{\text{tab}}} \sqrt{\frac{r_e \gamma \cos\theta\ t}{2\eta}}\right) & \text{for } t \in [0, \tau) \\ 1 & \text{for } t \in [\tau, \infty) \end{cases} \tag{21}$$

with $\tau = \min[H^2_{\text{tab}}\eta / 2r_e\gamma\cos\theta, 2R^2_{\text{tab}}\eta / r_e\gamma\cos\theta]$. The radial and axial wet front will advance simultaneously, and one or both will reach the center of the tablet, depending on the tablet's dimensions. τ is the minimum between the arrival time of the two wet fronts to reach the center of the tablet. Now, the rate of wetting is expressed as

$$\dot{\mathcal{W}}_{\text{API}}(t) = \begin{cases} \sqrt{\frac{r_e \gamma \cos\theta}{2\eta\ t}} \left(1 - \frac{1}{R_{\text{tab}}} \sqrt{\frac{r_e \gamma \cos\theta\ t}{2\eta}}\right) \times \left(\frac{1}{H_{\text{tab}}} + \frac{1}{R_{\text{tab}}} - \frac{3}{R_{\text{tab}} H_{\text{tab}}} \sqrt{\frac{r_e \gamma \cos\theta\ \tau}{2\eta}}\right) & \text{for } t \in [0, \tau) \\ 0 & \text{for } t \in [\tau, \infty) \end{cases} \tag{22}$$

For formulations that exhibit disintegration upon water uptake, tablet wetting functions endowed with disintegration events that, in turn, would speed up the API wetting process are desirable. However, such considerations fall outside the scope of this paper. These events, specifically the formation of cracks inside the tablets during the wetting process, have been experimentally observed by Ferdoush et al. (2023) using time-resolved micro-CT tests.

4. A two-stage mechanistic reduced-order model of pharmaceutical tablet dissolution

In this section, we will present the two-stage tablet dissolution ROM by coupling the API dissolution function $\mathcal{M}_{\text{API}}(t)$ and the tablet wetting function $\mathcal{W}_{\text{API}}(t)$. We will show how to numerically solve the tablet dissolution ROM and discuss the parameter identification method adopted.

The expression for the mechanistic API dissolution model for the dissolution of loose API crystal, as shown in Eq. (9), implies that all API mass becomes wet at $t = 0$. For tablet dissolution, the outer surface of the tablet becomes wet first, and eventually, so does the entire tablet. Tablet wetting is a time-dependent phenomenon, which depends on the manufacturing process conditions employed, such as lubrication and tablet porosity, among others. Thus, we obtain the two-stage tablet dissolution ROM by coupling the mechanistic API dissolution model and the tablet wetting function by means of convolution in time (Hayashi

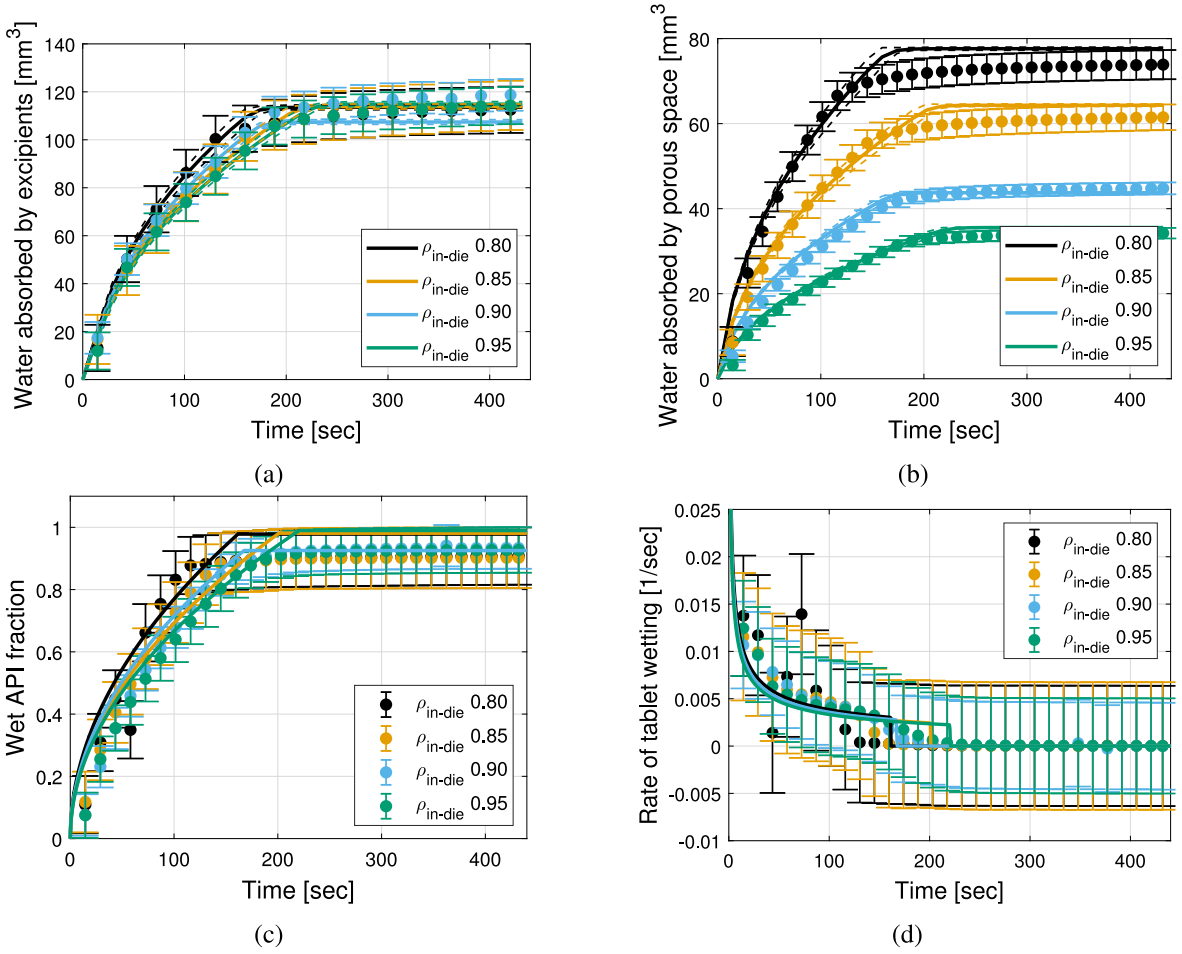

Fig. 2. Water absorption plots and wetting kinetics of the tablet obtained from Ferdoush et al. (2023). Circles denote experimental data, while lines represent predictions. The 95% confidence interval of the prediction is denoted by the dashed curves. (a) Water inside the excipients (using Eq. (14)). (b) Water inside the porous space (using Eq. (15)). (c) Wet API fraction as a function of time (using Eq. (17)). The experimental data of wet API fraction is obtained by using $\mathcal{W}_{\text{API}}(t) = 1 - V_{\text{dry}}(t)/V_{\text{total}}(0)$, where $V_{\text{total}}(0)$ is the initial tablet volume and $V_{\text{dry}}(t)$ is the tablet's dry portion volume. (d) Rate of wetting as a function of time (using Eq. (18)). The experimental data of the rate of wetting is obtained by using $\dot{\mathcal{W}}_{\text{API}}(t) = -\dot{V}_{\text{dry}}(t)/V_{\text{total}}(0)$.

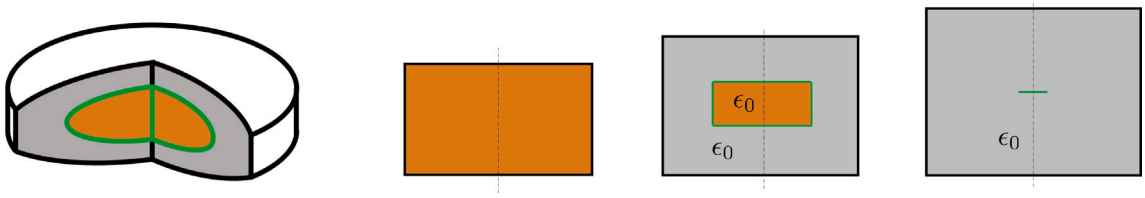

Fig. 3. A simplified diagram of dry and wet/swollen tablet. The color orange indicates the dry tablet, while gray signifies the tablet in its wet and swollen state. The radial and axial liquid front will meet depending on the dimension of the tablet. The green lines indicate a liquid front.

et al., 1995) to capture the start time of the API dissolution process as water uptake, swelling, and disintegration takes place. The fraction of drug released to the dissolution medium $M(t)$ is then expressed as follows

$$\begin{aligned} M(t) &= m_{\text{API}}^{\text{tab}} \int_0^t \dot{\mathcal{W}}_{\text{API}}(\hat{t})\mathcal{M}_{\text{API}}(t-\hat{t})\mathrm{d}\hat{t} \\ &= m_{\text{API}}^{\text{tab}} \int_0^t \underbrace{\dot{\mathcal{W}}_{\text{API}}(\hat{t})}_{\text{rate of API wetting}} \underbrace{3k_{\text{API}} \int_{\hat{t}}^t \int_0^\infty \frac{1}{\mu_3} L^2 n_{\text{m}}(L, \tau - \hat{t})\,\mathrm{d}L\,\mathrm{d}\tau}_{\text{pure API dissolution}}\ \mathrm{d}\hat{t} \end{aligned} \tag{23}$$

where $m_{\text{API}}^{\text{tab}}$ is the total mass of API inside the tablet.

4.1. Numerical solution

Eq. (23) is a convolution between the rate of API wetting and the pure API dissolution function. For a given time step size Δt, the HR-FVM discussed in Section 2 is used to find the dissolution profile for pure API at discrete times k. Similarly, the rate of tablet wetting, i.e., Eq. (22), is evaluated at discrete times k. Hence, the discretization of Eq. (23) takes the following form

$$M^k = m_{\text{API}}^{\text{tab}} \Delta t \left(\dot{\mathcal{W}}_{\text{API}}^k * \mathcal{M}_{\text{API}}^k \right) \tag{24}$$

where $*$ denotes the numerical convolution between two functions evaluated at discrete times k. The MATLAB (MATLAB version 9.8.0.1380330 (R2020a), 2020) environment is utilized to perform the

numerical convolution. MATLAB function `conv` was used in this case with the default algorithm.

4.2. Model parameter identification

The parameter identification method used in this study is a nonlinear multivariate maximization problem developed by Ferdoush and Gonzalez (2023). The method uses the similarity factor f_2 as outlined in the dissolution guidance document provided by the FDA (FDA and CDER, 1997). According to the guidance, two dissolution profiles are considered similar if $f_2 = 100$ and equivalent if $f_2 > 50$. In particular, the approach chooses optimal model parameters $\bar{\mathcal{P}}$ and aims to maximize the similarity factor f_2 (or minimize $100 - f_2$) between the model predictions $\mathcal{M}^i$ and the experimental dissolution data $\mathcal{E}^i$, that is

$$\bar{\mathcal{P}} = \arg\min_{\mathcal{P}\in\mathcal{R}_+} \Phi(\mathcal{P}) = \arg\min_{\mathcal{P}\in\mathcal{R}_+} \sum_{i=1}^{S} 100 - f_2(\mathcal{M}^i(\mathcal{P}) - \mathcal{E}^i) \tag{25}$$

The error measurement functions are defined based on the similarity factor

$$f_2(\mathcal{M}^i - \mathcal{E}^i) = 50 \log\left\{100\left[1 + \frac{1}{N_i}\|\mathcal{M}^i - \mathcal{E}^i\|^2\right]^{-0.5}\right\} \tag{26}$$

where S is the number of experimental dissolution data sets, $\|\cdot\|$ is the L2-norm, N_i is the number of data points in the ith experimental set, and the model parameters' set is expressed as

$$\mathcal{P} \equiv \{k_{\text{API}}, r_e(\epsilon)\} \tag{27}$$

The MATLAB environment is utilized to solve the nonlinear multivariate minimization problem (MATLAB version 9.8.0.1380330 (R2020a), 2020). MATLAB constrained optimization function `fmincon` was used in this case with the default algorithm (interior-point).

The bootstrapping method was adopted to obtain the median and 68% confidence interval of the estimated model parameters. First, we generate multiple (1000) bootstrap samples by randomly sampling from the original experimental dataset (percentage of drug dissolved) by assuming that the experimental error follows a normal distribution with a 68% confidence interval lying within the experimental error bound. Each bootstrap sample was the same size as the original dataset. For each bootstrap sample, parameter estimation was performed by following the procedure described in the above paragraph. Next, outliers were removed from these estimated parameters by using MATLAB function `rmoutliers` with the default algorithm, and the median and 68% confidence interval were determined for each parameter. We illustrate this procedure in the next section.

5. Examples of application

The mechanistic API dissolution model and the two-stage tablet dissolution model correlate dissolution profiles with CPPs, CMAs, and other crucial CQAs. We demonstrate the versatility and effectiveness of the models in predicting the dissolution profiles of diverse pharmaceutical formulations and their correlation with initial API crystal size distribution, composition, tablet dimensions, and porosity through the following case studies:

1. Characterization of acetaminophen crystals
2. Dissolution prediction of acetaminophen tablets
3. Characterization of lomustine crystals
4. Dissolution prediction of lomustine tablets

Model parameters (27) for the proposed dissolution models, i.e., Eqs. (9), (22) and (23), are estimated using the parameter identification method as described in Section 4.2.

Table 1
Parameters of the population balance model for APAP powder dissolution.

Property	Unit	Value	Estimation
m_{API}	mg	13.16	–
ρ_{API}	kg/m^3	1293	–
V_{D}	m^3	0.0009	–
k_{API}	μm/min		30.9

5.1. Characterization of acetaminophen crystals

Acetaminophen (APAP) powders were obtained from Mallinckrodt Pharmaceuticals, US. Sieve analysis was performed using a Tyler ro-tap model E test sieve shaker to obtain a CSD between 0–355 μm. Next, sampling was performed on the sieved APAP powders. APAP powder was poured into the Retsch PT100 spinning riffler equipment hopper using a scoop to obtain eight smaller sub-samples. One of the eight samples was then again divided into eight sub-samples using the spin riffler. This procedure was repeated until a representative sample size was obtained to perform morphology analysis and dissolution test. Next, morphology analysis was performed using a Malvern G3SE-ID particle size and shape analyzer on the sieved APAP sample to obtain the particle size and shape data. A Vankel dissolution apparatus of model VK 7000 was used to perform dissolution tests on the crystals. The dissolution apparatus had an auto-sampling manifold of model VK 8000. Dissolution tests were performed on 13.16 mg sieved APAP samples in a 900 mL phosphate buffer media of pH 5.8 at temperature 37 ± 0.5 °C for 90 min. Three replicates were performed for each experiment. The experiments utilized a USP II apparatus (paddle apparatus, see USP (2011) for more details) running at 50 rpm, while the absorbance of the API was assessed at 243 nm in a Cary-60 UV–Vis spectrophotometer.

The mechanistic API dissolution model, Eq. (9), was used to estimate the dissolution rate k_{API} from the experimental dissolution data of APAP powders. The value of Δt and ϵ used for the HR-FVM calculations as described in Section 2.1 were 0.01 min and 1×10^{-16}, respectively. The model parameters used for estimating k_{API} were selected in accordance with the experimental method (see Table 1). The parameter estimation was performed following the method described in Section 4.2. Figs. 4(a) and 4(b) show the initial number-based distribution and contour plot of the APAP particles. The contour plot shows that the normalized CSD function $n_{\text{m}}(L,t)$ diminishes with time by following linear characteristic lines, in turn, the crystal size distribution changes with time. The prediction of the model is shown in Fig. 4(c). A similarity value f_2 between prediction and experimental dissolution data above 50 indicates that dissolution profiles are equivalent (FDA and CDER, 1997) and, thus, that the prediction is acceptable.

If a size-dependent dissolution rate is considered, i.e., Eq. (6), the similarity factor improves marginally to 59.91 from 56.95, and thus, such dependency is neglected for APAP. Similarly, the effect of particle shape may also be considered (Lu et al., 1993). Ghazi et al. (2019) investigated the shape of APAP powders using scanning electron microscopy (SEM), and they observed that APAP particles have rod or needle-like shapes. This observation suggests that under the assumption of rod-like crystals, the surface area to volume ratio would be higher than for spherical geometries, and so would be the rate of dissolution (as it is the case of the experimental data in Fig. 4(c)). However, the extension of the dissolution model presented in Section 2 to rod-like particles is not addressed within the scope of this paper.

5.2. Dissolution prediction of acetaminophen tablets

Acetaminophen tablets of four different in-die relative densities $\rho_{\text{in-die}}$ (0.8, 0.85, 0.9, and 0.95) were made in a bench top compactor simulator of Gamlen D-Series with a flat punch and a 6 mm die. The in-die relative densities were attained by adjusting tablet thickness

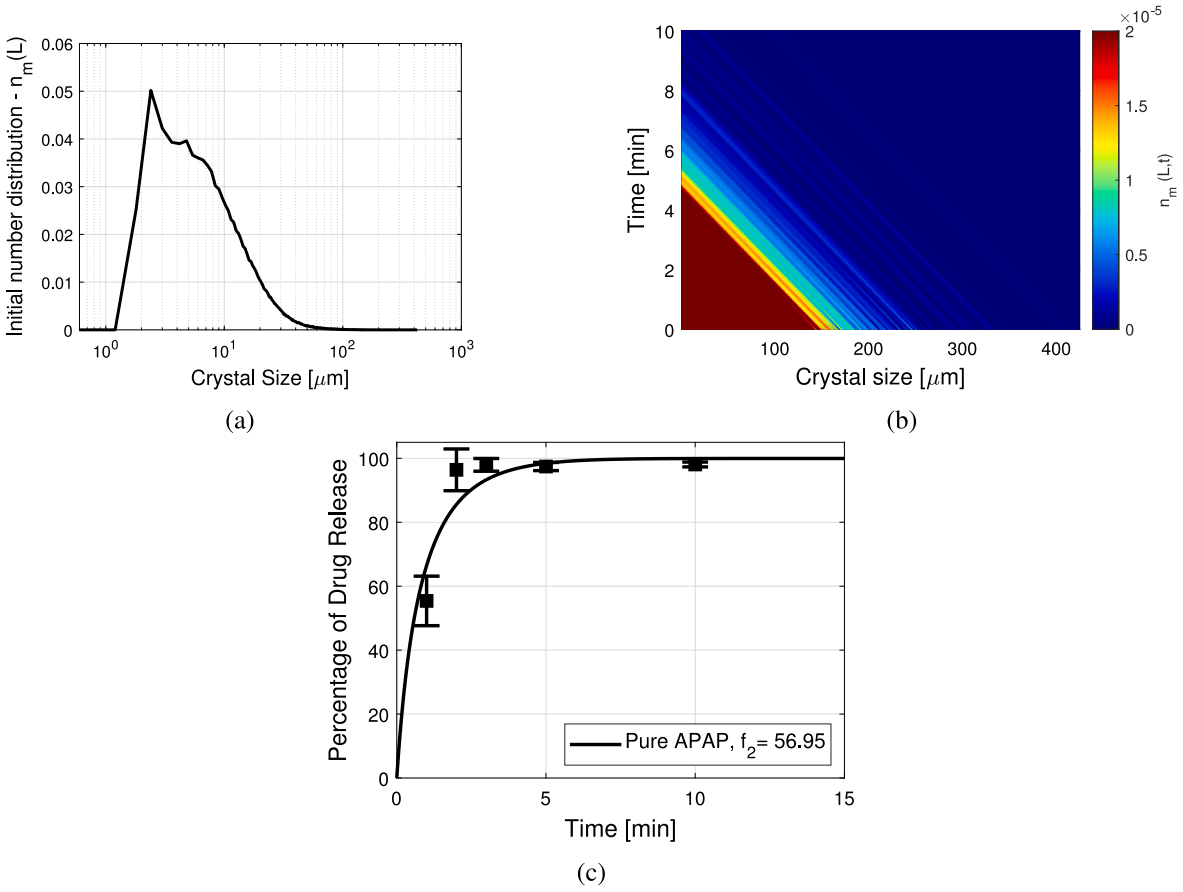

Fig. 4. The mechanistic API dissolution model, Eq. (9) fitted to APAP powder's dissolution data, estimated parameter $k_{API} = 30.9$ μm/min. Standard deviation is calculated from three sets of dissolution data. (a) Initial number-based distribution of APAP powder. (b) Contour plot of APAP powder. (c) Model prediction and APAP powder's dissolution data.

and targeting a weight of 153 mg. Three sets of tablets were made by varying the API concentration. The tablet formulation comprised 81%, (89%, and 96%) microcrystalline cellulose (MCC, Avicel PH 200), 17%, (9%, and 2%) acetaminophen, 1% magnesium stearate, and 1% colloidal silica dioxide, all % w/w. Acetaminophen was obtained from Mallinckrodt Pharmaceuticals, US, MCC was obtained from DuPont Nutrition, US, magnesium stearate was obtained from Spectrum Chemical Mfg. Corp., New Brunswick, NJ, US, and silica was obtained from Cabot Corporation, IL, US.

Powders for fabricating 15 tablets of each formulation were premixed manually in small batches in a 20 ml glass vial. The powders were mixed for 10 min. After the tablets were ejected from the die, the tablet porosity ϵ_0, as shown in Table 3, was determined from the true density of the powder blend, tablet volume, and mass. The true density of the blend ρ_{true} (reported in Table 2) was calculated from the true densities ρ_i and mass fractions x_i of its individual components using a mixture rule (Sun, 2004), i.e.,

$$\rho_{true} = 1/\sum(x_i/\rho_i) \tag{28}$$

The true density of the individual component was obtained from the manufacturer. Next, dissolution tests were performed on the tablets in a 900 mL phosphate buffer media of pH 5.8 at temperature 37 ± 0.5 °C for 90 min. A Vankel dissolution apparatus of model VK 7000 was used to perform dissolution tests on the tablets. The dissolution apparatus had an auto-sampling manifold of model VK 8000. Three replicates were performed for each experiment. The experiments utilized a USP II apparatus running at 50 rpm, while the absorbance of the API was assessed at 243 nm in a Cary-60 UV–Vis spectrophotometer.

Table 2
Properties of the liquid and the powder blend (Markl et al., 2017; Steele et al., 2008; Ferdoush and Gonzalez, 2023). The contact angle θ between Avicel PH101 and water is determined by Steele et al. (2008) using capillary intrusion experiments. The true density of the powder blend of different APAP formulations with varying API concentrations is also listed. The contact angle θ may change due to particle coating and lubrication conditions (Kristó et al., 2010).

Property	Unit	Value
γ	N/m	72.3×10^{-3}
θ		64.3°
η	Pa s	1.002×10^{-3}
ρ_{true} (17% APAP)	kg/m^3	1414
ρ_{true} (9% APAP)	kg/m^3	1427
ρ_{true} (2% APAP)	kg/m^3	1437

Estimation of the model parameters is performed by following the steps described in Section 4. Specifically, by leveraging the characteristics of the liquid, the powder blend, and the tablet (see Tables 2 and 7), Eq. (23) is used with the experimental data in Figs. 5(a), 5(c) and 5(e), respectively, to estimate model parameters r_e. A set of model parameters is estimated to obtain a median and 68% confidence interval of r_e following the bootstrapping method discussed in Section 4.2. Since the distribution of r_e is skewed, we have reported the median of r_e instead of the mean in Table 3. The value of Δt and ϵ used for the HR-FVM calculations as described in Section 2.1 were 0.01 min and 1×10^{-16}, respectively. The mass of API in each tablet was obtained from the experimental dissolution data as shown in Table 7 in the Appendix. For a specific formulation, the mass of API in tablets of same and different porosity vary slightly as shown in Figs. 5(b), 5(d) and 5(f). It is worth

Table 3
The median and 68% confidence interval of estimated effective capillary radius of tablets of three different formulations with varying APAP concentrations (i.e., 17% APAP, 9% APAP, and 2% APAP).

In-die-porosity	17% APAP		9% APAP		2% APAP	
	Tablet porosity	Estimated r_e (nm)	Tablet porosity	Estimated r_e (nm)	Tablet porosity	Estimated r_e (nm)
0.95	0.28 ± 0.004	3.74 [2.07, 7.19]	0.30 ± 0.005	3.45 [2.53, 5.88]	0.31 ± 0.002	5.75 [5.53, 5.99]
0.9	0.33 ± 0.009	11.35 [7.39, 21.67]	0.32 ± 0.026	8.79 [4.99, 18.68]	0.33 ± 0.005	7.16 [6.96, 7.34]
0.85	0.35 ± 0.006	11.32 [7.73, 19.21]	0.37 ± 0.012	16.57 [9.74,29]	0.36 ± 0.004	7.45 [6.34, 9.67]
0.8	0.39 ± 0.002	8.71 [5.12, 16.45]	0.39 ± 0.002	5.49 [3.32, 13.31]	0.40 ± 0.005	12.45 [10.01, 19.12]

mentioning that r_e was estimated using experimental dissolution data points at times in $[0, 5\tau]$, with τ being the tablet wetting time $\tau = \min[H_{\text{tab}}^2, 4R_{\text{tab}}^2] \times \eta / 2 r_e \gamma \cos\theta$ (see Eq. (22)). For example, if the tablet wetting time was within one minute, experimental dissolution data points until 5 min were used to estimate r_e. The more data points there are before the tablet wetting time, the more accurate the estimation of r_e. Model parameter k_{API} was directly used from the estimated value in Section 5.1. The accuracy of the estimation is evidenced by similarity factor values surpassing 50 for each pair of predicted and experimental dissolution profiles, in accordance with the guidelines (FDA and CDER, 1997) (see Fig. 5).

The estimated effective capillary radii r_e with 68% confidence interval are also shown as a function of tablet porosity in Fig. 6(a). It is worth mentioning that capillary radius values have a wider confidence interval at high porosity, suggesting perhaps that the dissolution profiles are not very sensitive to capillary radius values since water uptake is very fast at high porosity and dissolution is mainly controlled by CSD of the API. However, wide confidence intervals can also be attributed to a small sample size. Despite of these statistical observations, it is evident from the figure that capillary radius has an increasing trend with respect to tablet porosity and an apparent lack of dependency on APAP concentration. This trend is captured by the following exponential equation

$$r_e(\epsilon) = r_{\epsilon_c} \exp\left(a \frac{\epsilon - \epsilon_c}{\epsilon}\right) \text{ for } \epsilon = [0, \epsilon_c] \tag{29}$$

where ϵ_c is the tensile strength critical porosity, i.e., the maximum porosity achievable during tablet formation. The tensile strength critical porosity ϵ_c is obtained from diametrical compression tests or tablet hardness tests by fitting the Leuenberger equation (see, e.g., Razavi et al. (2018)) to the tensile strength data of tablets of different tablet porosities, that is from

$$\sigma_t(\epsilon) = \sigma_0 \left[1 - \frac{\epsilon}{\epsilon_c} e^{(\epsilon_c - \epsilon)}\right] \text{ for } \epsilon = [0, \epsilon_c] \tag{30}$$

where σ_0 represents the tensile strength of a fully compacted tablet, meaning a tablet with no porosity. At ϵ_c, the effective capillary radius r_{ϵ_c} is large, the wetting time short, and the dissolution profile equivalent to the one of the loose powder blend, i.e., to the one of pure API (Ferdoush and Gonzalez, 2023). For APAP tablets, the tensile strength critical porosity is $\epsilon_c = 0.43$ and $\sigma_0 = 5.3$ MPa from Eq. (30) and, from Eq. (29), $r_{\epsilon_c} = 9.75$ nm and $a = 0.36$. Interestingly, the capillary radius values reported by Ferdoush et al. (2023) for the same formulation are also in good agreement with this trend (see the 9% APAP values added to Fig. 6(a)).

It is evident from Figs. 5 and 6(b) that, for this APAP-MCC formulation, tablet porosity does have a weak effect on dissolution profile, while it strongly controls the tensile strength. Specifically, for different APAP concentrations and tablet porosities, wetting kinetics is quite fast (1–5 min) due to the high concentration of MCC, a disintegrant (Rowe et al., 2009; Bhalekar et al., 2010), and, in turn, dissolution is controlled by the API dissolution function $\mathcal{M}_{\text{API}}$. Fig. 7 shows the tablet wetting function $\mathcal{W}_{\text{API}}$ (Eq. (21)), with vertical lines at the tablet wetting time τ, i.e., at the time when the tablet is entirely wet. At low porosity, the wetting time is higher and thus porosity plays a role in delaying API dissolution. It bears emphasis that the two-stage mechanistic ROM is capable of decoupling these effects and automatically making CSD and k_{API} the model parameters that dominate the tablet dissolution profile. In contrast, for other formulations, such as the one resulting from adding lactose to APAP-MCC mixtures (Callegari et al., 2013) or the one with APAP and lactose (Callegari et al., 2013), the wetting process would be slower and, as a result, the two stages of the ROM would balance out. A case in point will be the example presented next.

It is worth mentioning that capillary radius values have a high confidence interval at high porosity, indicating that the dissolution profiles are not very sensitive to capillary radius values since water uptake is very fast at high porosity.

Table 4
Parameters of the population balance model for lomustine crystal dissolution.

Property	Unit	Value	Estimation
m_{API}	mg	5	–
ρ_{API}	kg/m^3	1400	–
V_{D}	m^3	0.0009	–
k_{API}	μm/min		1.9

5.3. Characterization of lomustine crystals

Lomustine crystals manufactured at Purdue University using a novel small-scale hybrid manufacturing system by Mackey et al. (2020) were employed in this study. Firstly, morphology analysis was performed using a Malvern G3SE-ID particle size and shape analyzer on a batch of crystals with a wide CSD (0–1179 μm). Next, sieve analysis was performed using a Tyler ro-tap model E test sieve shaker, and the following five sieved fractions of particles were obtained: (i) CSD: 0–180 μm, (ii) CSD: 180–250 μm, (iii) CSD: 125–250 μm, (iv) CSD: 250–355 μm, and (v) CSD: 250–500 μm. Since lomustine was manufactured in very small batches, a scoop was used to perform sampling to obtain the desired amount of lomustine for dissolution tests. Lastly, for each sieved fraction, dissolution experiments were conducted on 5 mg samples in pH 6.8 phosphate buffer media (1% surfactant, sodium lauryl sulfate added) at a temperature of 37 ± 0.5 °C for a duration of 90 min (Ferdoush and Gonzalez, 2023). A Vankel dissolution apparatus of model VK 7000 was used to perform dissolution tests on the crystals. The dissolution apparatus had an auto-sampling manifold of model VK 8000. The media volume was 900 mL. Three replicates were performed for each experiment. The experiments utilized a USP II apparatus running at 75 rpm, while the absorbance of the API was assessed at 231 nm in a Cary-60 UV–Vis spectrophotometer

The mechanistic API dissolution model, Eq. (9), was used to estimate the dissolution rate k_{API} from the experimental dissolution data of lomustine crystal. The value of Δt and ϵ used for the HR-FVM calculations as described in Section 2.1 were 0.2 min and 1×10^{-16}, respectively. The model parameters used for the estimation of k_{API} were selected according to the experimental methodology (see Table 4). The true density of lomustine can be found experimentally using a gas pycnometer (Sun, 2004); however, in this work, the density of lomustine shown in Table 4 is obtained from Lomustine. Chemsrc. (n.d.) (2024). The parameter estimation was conducted in accordance with the procedure outlined in Section 4.2. Figs. 8(a) and 8(b) show the initial number-based distribution and contour plot of the lomustine crystal. The contour plot shows that the normalized CSD function

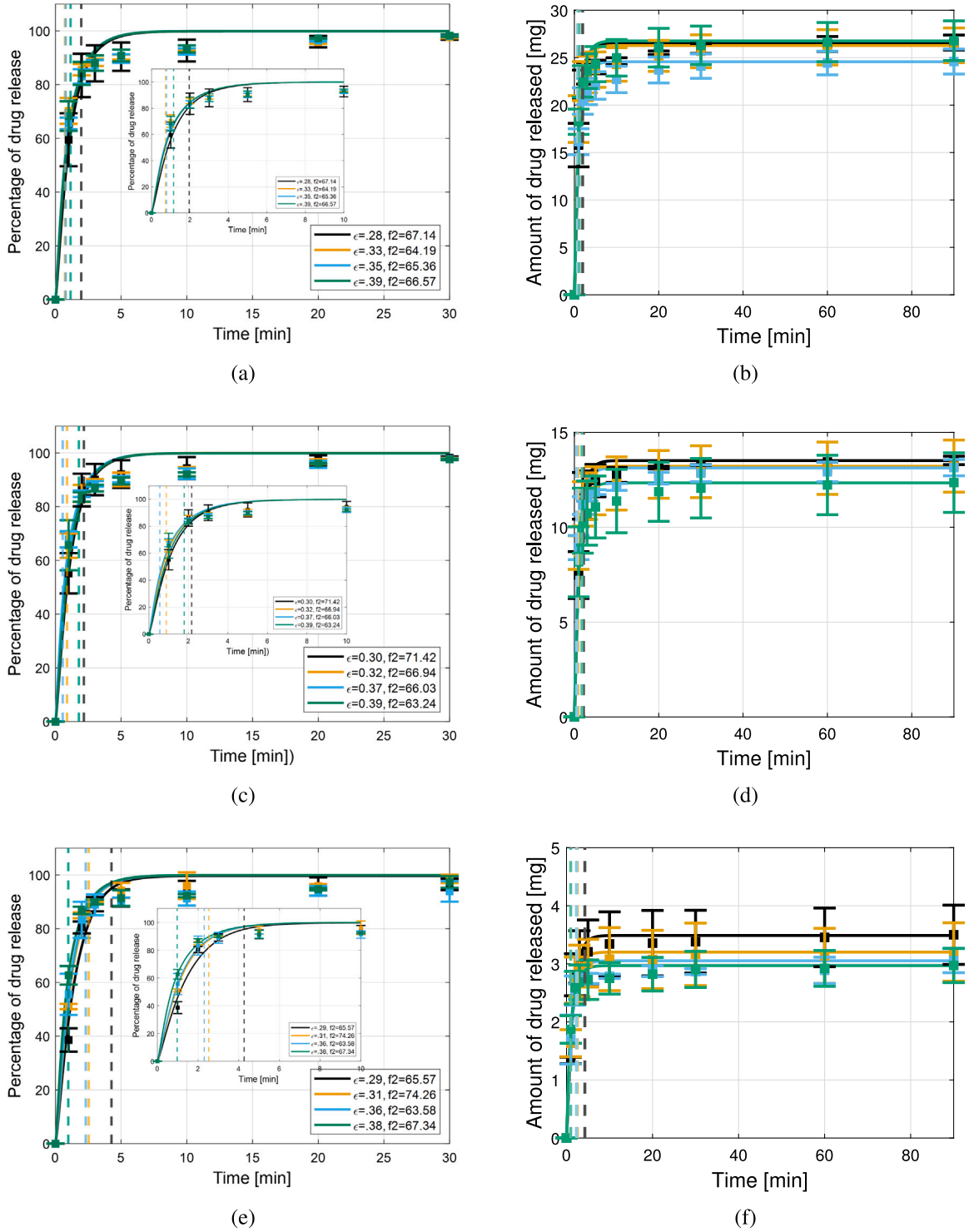

Fig. 5. Effect of porosity on APAP tablet's dissolution and concentration profiles. Inserts depict dissolution data at earlier time points. Squares represent experimental data, and lines represent predictions. Standard deviation is calculated from three sets of dissolution data. The vertical dotted lines indicate the time scale when the tablet is fully wet. Dissolution profiles of formulation consisting of (a) 17% APAP, 81% MCC, 1% MgSt, 1% Cab-O-Sil, (c) 9% APAP, 89% MCC, 1% MgSt, 1% Cab-O-Sil (same formulation as used by Ferdoush et al. (2023)), and (e) 2% APAP, 96% MCC, 1% MgSt, 1% Cab-O-Sil. Concentration profiles of formulation consisting of (b) 17% APAP, 81% MCC, 1% MgSt, 1% Cab-O-Sil, (d) 9% APAP, 89% MCC, 1% MgSt, 1% Cab-O-Sil, and (f) 2% APAP, 96% MCC, 1% MgSt, 1% Cab-O-Sil.

$n_m(L,t)$ diminishes with time by following linear characteristic lines, in turn, the crystal size distribution changes with time. The prediction of the model is shown in Fig. 8(c). A similarity value f_2 between prediction and experimental dissolution data above 50 indicates that dissolution profiles are equivalent (FDA and CDER, 1997) and, thus, that the prediction is acceptable.

As expected, Fig. 8(c) shows that dissolution becomes faster for sieved fractions with decreasing crystal size. Furthermore, it also shows that the standard deviation in the measured values is high for sieved fractions with increasing crystal size. This variability can arise due to sampling variations. Interestingly, this in-batch variability can readily be estimated using the mechanistic API dissolution model proposed in

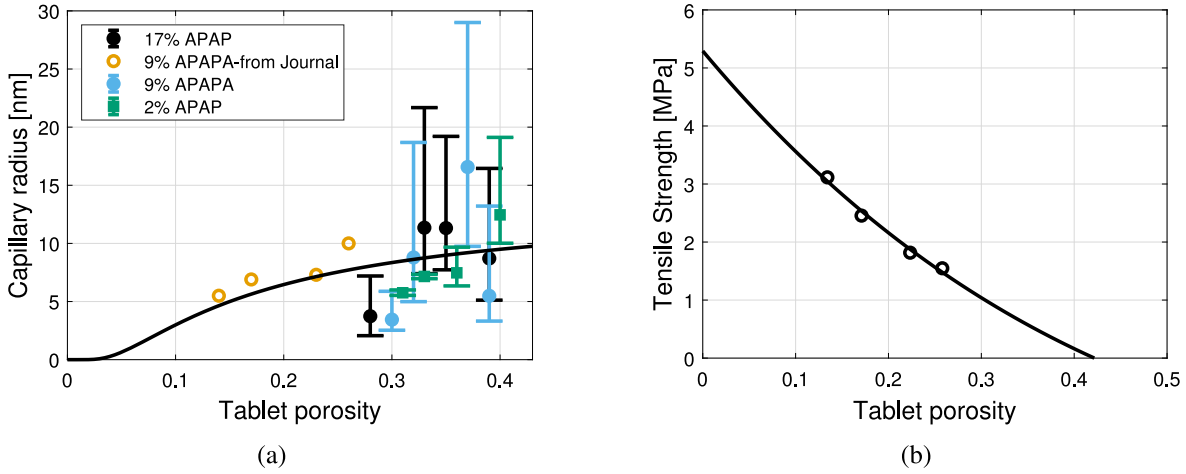

Fig. 6. Trend of capillary radius and tensile strength with respect to tablet porosity. Circles denote experimental data, while lines denote model predictions. (a) The trend of the capillary radius with respect to tablet porosity for APAP tablets. The error bars indicate 68% confidence interval of the estimated capillary radius values. The orange data points are obtained from the estimated capillary radius values reported by Ferdoush et al. (2023). (b) The trend of tensile strength with respect to tablet porosity for formulation with 9% APAP.

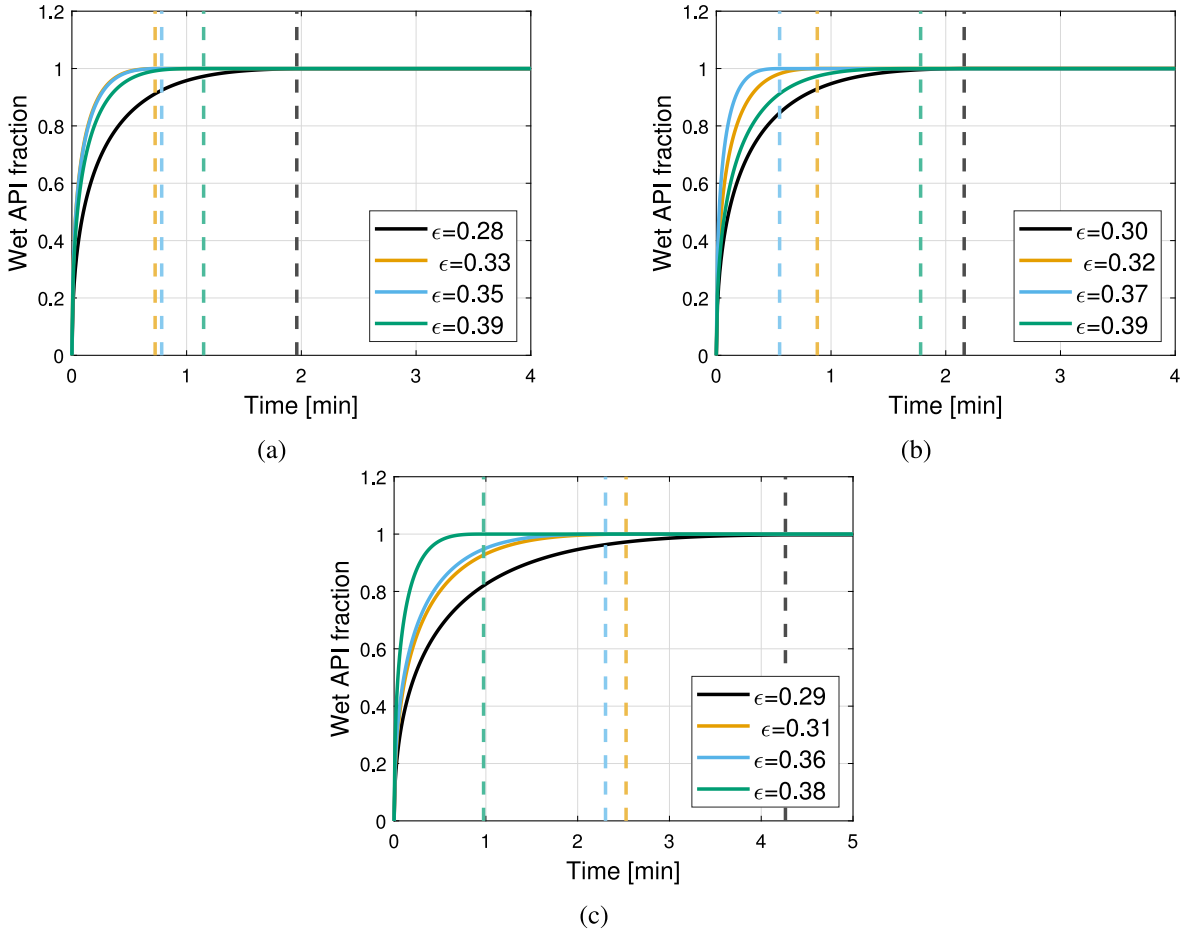

Fig. 7. Tablet wetting kinetics, wet API fraction as a function of time. The vertical dotted lines indicate the time scale when the tablet is fully wet, or the wet API fraction is one. Formulation consists of (a) 17% APAP, 81% MCC, 1% MgSt, 1% Cab-O-Sil, (b) 9% APAP, 89% MCC, 1% MgSt, 1% Cab-O-Sil (same formulation as used by Ferdoush et al. (2023)), and (c) 2% APAP, 96% MCC, 1% MgSt, 1% Cab-O-Sil.

this work. By way of example, two size fractions are chosen, namely 0–1179 μm and 125–250 μm, and thirty 5-mg samples are numerically generated from the corresponding fractions of the experimentally measured CSD showed in Fig. 8(a). A sufficient number of particles were drawn and converted to mass by assuming a spherical shape. It was ensured that the numerically drawn particles did not exceed a mass of 5 mg. The distribution of the particles that constituted the 5 mg sample was used as an initial distribution for the HR-FVM described in Section 2.1. Then, using the k_{API} value shown in Table 4, dissolution profiles were generated for those thirty 5-mg samples by using

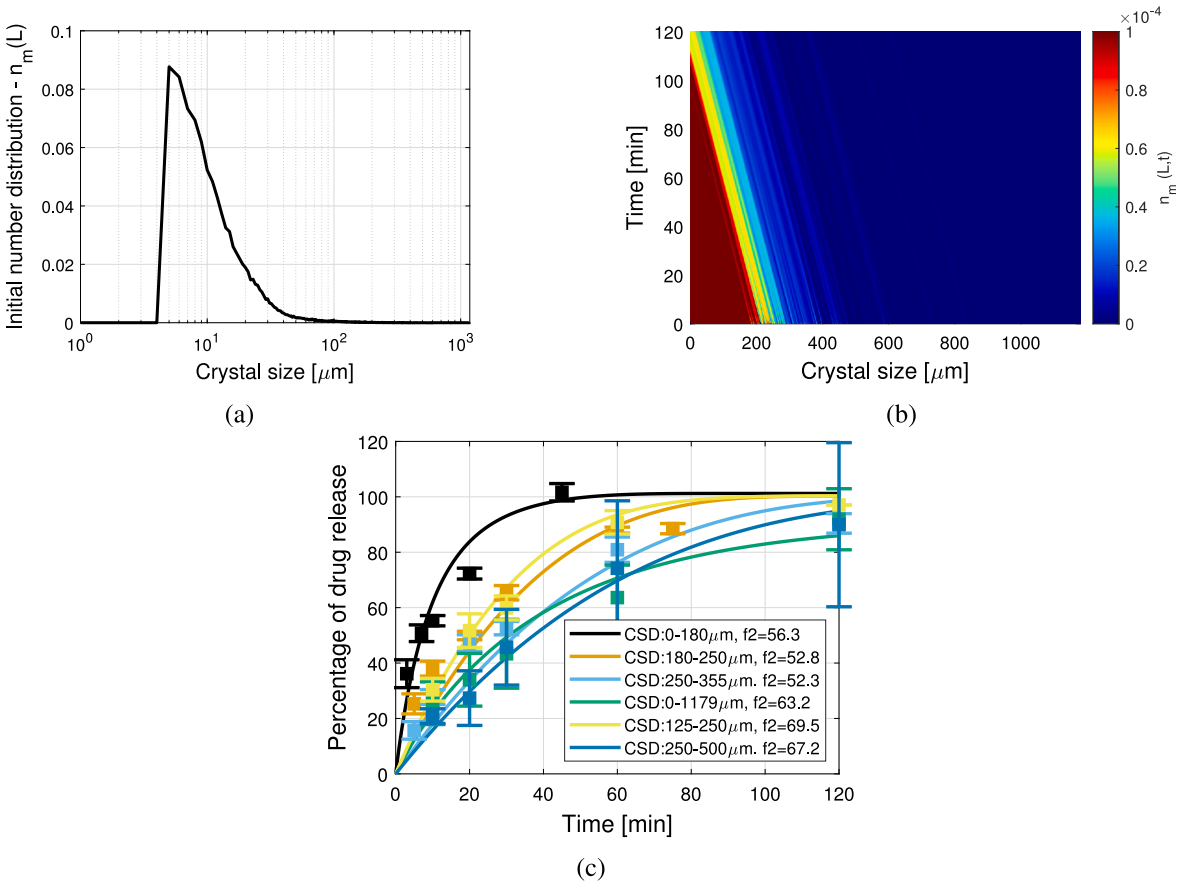

Fig. 8. The mechanistic API dissolution model, Eq. (9) fitted to lomustine crystal's dissolution data for six different CSD, estimated parameter k_{API} = 1.91 μm/min. Standard deviation is calculated from three sets of dissolution data of each CSD. (a) Initial number-based distribution of lomustine, CSD: 0–1179 μm. (b) Contour plot of lomustine crystal, CSD: 0–1179 μm. (c) PBM model prediction and lomustine crystal's dissolution data.

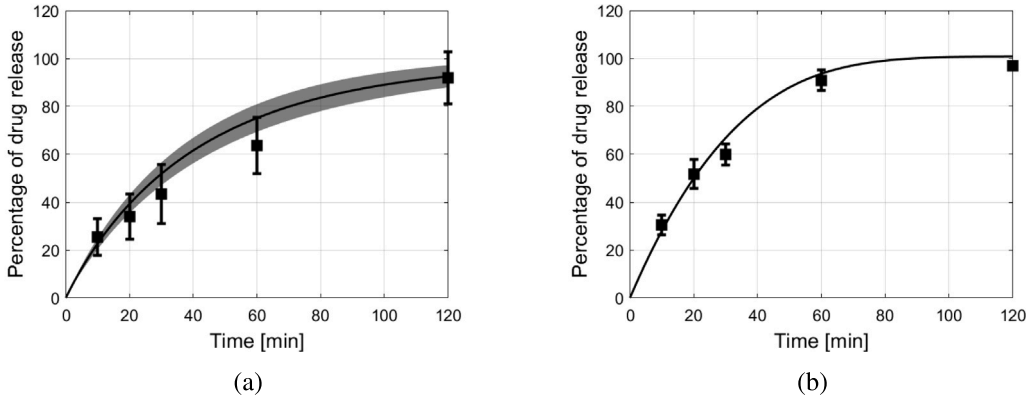

Fig. 9. In-batch variability prediction for 5 mg lomustine samples of (a) CSD 0–1179 μm. (b) CSD 125–250 μm. Squares denote experimental data, while lines denote model predictions. The experimental error bars are obtained from three sets of dissolution data. The shaded gray area represents the standard deviation obtained from model predictions.

Eq. (9). Next, mean and standard deviation values for those dissolution profiles are calculated. These results are reported in Fig. 9, and they are in remarkable agreement with the experimental data. It is worth mentioning that a similar analysis done with APAP crystals yields very small standard deviations—if information about shape distribution was available, the same methodology proposed here could be adopted.

5.4. Dissolution prediction of lomustine tablets

Two distinct batches of lomustine tablets were produced using CSD 0–180 μm and 125–250 μm. Tablets of four different in-die relative densities ρ_{in-die} (0.8, 0.85, 0.9, and 0.95) for CSD 0–180 μm and three different in-die relative densities ρ_{in-die} (0.85, 0.9, and 0.95) for 125–250 μm were made in a bench top compactor simulator of Gamlen D-Series with a flat punch and a 6 mm die. The in-die relative densities were attained by adjusting tablet thickness and targeting a weight of 114 mg. Three replicates were produced for each type of tablet. The tablet formulation comprised 70.59% w/w lactose monohydrate (Pharmatose), 24% w/w mannitol (D-mannitol), 4.41% w/w lomustine, and 1% w/w MgSt. Lactose was obtained from DFE pharma, mannitol from Sigma-Aldrich, and MgSt from Acros Organics.

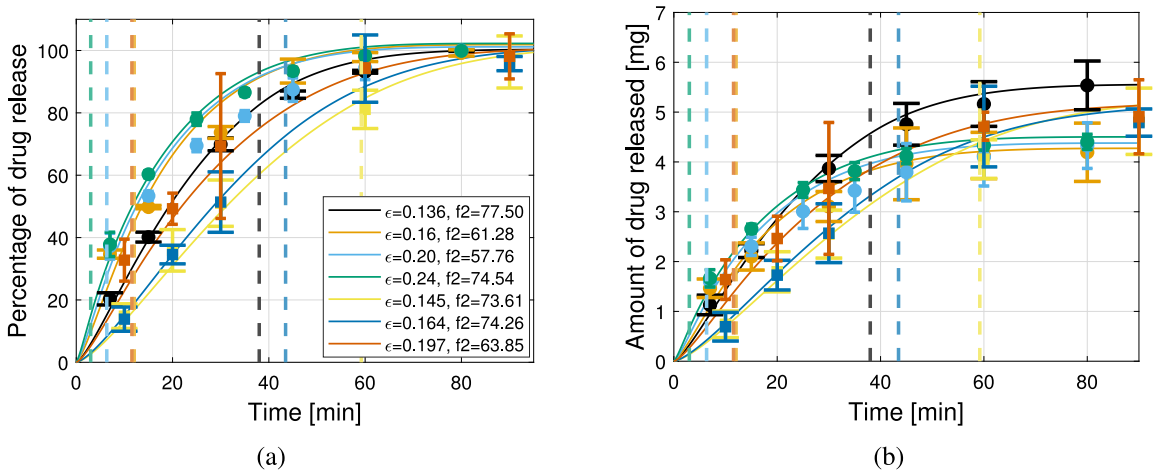

Fig. 10. Effect of porosity and CSD on lomustine tablet's dissolution data. Circles represent experimental data for CSD 0–180 μm, squares represent experimental data for CSD 125–250 μm, and lines represent predictions. Standard deviation is calculated from three sets of dissolution data. The vertical dotted lines indicate the time scale when the tablet is fully wet. (a) Dissolution profile. (b) Concentration profile.

Powders for fabricating 30 tablets of each type were mixed manually in small batches in a 20 ml glass vial. The powders were mixed for 10 min. After the tablets were ejected from the die, the tablet porosity ϵ_0, as shown in Table 6 was determined using the true density of the powder blend, along with the tablet volume and mass. The true density of the blend ρ_{true} was calculated from the true density and mass fraction of each individual component using the mixture rule Eq. (28). The true density of the individual component was obtained from the manufacturer. Next, dissolution tests were performed on the tablets in pH 6.8 phosphate buffer media (1% surfactant, sodium lauryl sulfate added) at a temperature of 37 ± 0.5 °C for a duration of 90 min (Ferdoush and Gonzalez, 2023). A Vankel dissolution apparatus of model VK 7000 was used to perform dissolution tests on the tablets. The dissolution apparatus had an auto-sampling manifold of model VK 8000. The media volume was 900 mL. Three replicates were performed for each experiment. The experiments utilized a USP II apparatus running at 75 rpm, while the absorbance of the API was assessed at 231 nm in a Cary-60 UV–Vis spectrophotometer.

Estimation of the model parameters is performed by following the steps described in Section 4. Specifically, utilizing the characteristics of the liquid, the powder blend, and the tablet (see Tables 5 and 8), Eq. (23) is used with the experimental data in Fig. 10(a) to estimate model parameters r_e. A set of model parameters is estimated to obtain a median and 68% confidence interval of r_e following the bootstrapping method discussed in Section 4.2. Since the distribution of r_e is skewed, we have reported the median of r_e instead of the mean in Table 6. The value of Δt and ϵ used for the HR-FVM calculations as described in Section 2.1 were 0.2 min and 1×10^{-16}, respectively. The mass of API in each tablet was obtained from the experimental dissolution data as shown in Table 8 in the Appendix. The mass of API in tablets of the same and different porosity varies slightly, as shown in Fig. 10(a). It is worth mentioning that r_e was estimated using experimental dissolution data points at times in $[0, 5\tau]$, with τ being the tablet wetting time (see Eq. (22)). For example, if the tablet wetting time was within one minute, experimental dissolution data points until 5 min were used to estimate r_e. The more data points there are before the tablet wetting time, the more accurate the estimation of r_e. Model parameter k_{API} was directly used from the estimated value in Section 5.3. The accuracy of the estimation is evidenced by similarity factor values surpassing 50 between each pair of predicted and experimental dissolution profiles, in accordance with the guidelines (FDA and CDER, 1997) (see Fig. 10).

The estimated effective capillary radii r_e with 68% confidence interval are also shown as a function of tablet porosity in Fig. 11. Capillary radius values have narrow confidence intervals at low porosity, whereas at high porosity, the confidence interval is wider. Capillary radius has an increasing trend with respect to tablet porosity. This trend is captured by Eq. (29). Ferdoush and Gonzalez (2023) reported 0.23 as the tensile strength critical porosity for lomustine tablets made of API CSD of 125–250 μm. However, we also have tablets made of API CSD of 0–180 μm. Thus, the tensile strength critical porosity value for these new tablets may change compared to the reported values in the literature. From Eq. (29), $r_{\epsilon_c} = 17.64$ nm and $a = 4.74$. The model prediction aligns well with the experimental data (see Fig. 11).

It is clear from Fig. 10 that both porosity of the tablet and API CSD affect dissolution profiles for lomustine tablets. Specifically, wetting kinetics is dependent on tablet porosity; in turn, dissolution is controlled by both tablet wetting function $\mathcal{W}_{\text{API}}$ and the API dissolution function $\mathcal{M}_{\text{API}}$. Fig. 12 shows the tablet wetting function $\mathcal{W}_{\text{API}}$ (Eq. (21)), with vertical lines at the tablet wetting time τ, i.e., the time when the tablet is completely wet. For all the tablets with higher porosity, the wetting time is faster compared to the tablets with lower porosity with higher wetting time due to smaller r_e values. It bears emphasis that the two-stage mechanistic ROM is capable of coupling these effects and

Table 5
Properties of the liquid (Markl et al., 2017; Steele et al., 2008; Ferdoush and Gonzalez, 2023) and the powder blend (Depalo and Santomaso, 2013). The contact angle θ may change due to particle coating and lubrication conditions (Kristó et al., 2010). The contact angle is between lactose monohydrate and a liquid of lactose saturated solution (Depalo and Santomaso, 2013). Other ingredients in the tablet may affect the contact angle.

Property	Unit	Value
γ	N/m	72.3×10^{-3}
θ		88.2°
η	Pa s	1.002×10^{-3}
ρ_{true}	kg/m^3	1530

Table 6
The median and 68% confidence interval of the estimated effective capillary radius of lomustine tablets. The standard deviation values reported for tablet porosity are calculated from three data sets.

CSD (μm)	Target in-die-porosity	Tablet porosity	Estimated r_e (nm)
0–180	0.95	0.136 ± 0.006	0.89 [0.81, 0.97]
	0.9	0.16 ± 0.001	2.94 [2.17, 4.45]
	0.85	0.2 ± 0.005	6.21 [3.83, 10.05]
	0.8	0.24 ± 0.005	14.56 [7.89, 21.83]
125–250	0.95	0.145 ± 0.001	0.59 [0.46, 0.82]
	0.9	0.164 ± 0.001	0.82 [0.57, 1.15]
	0.85	0.197 ± 0.002	3.42 [0.92, 6.97]

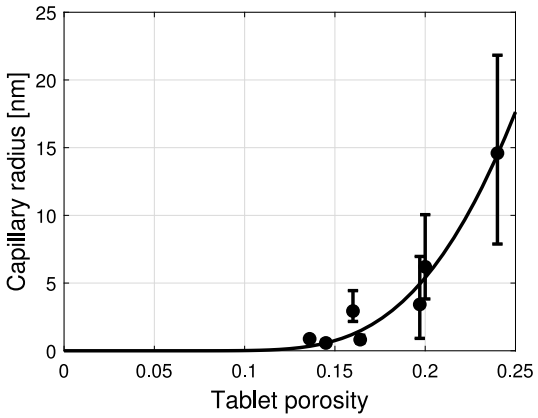

Fig. 11. Trend of capillary radius with respect to tablet porosity for lomustine tablets. Circles denote experimental data, and line denotes model prediction. The error bars indicate 68% confidence interval of the estimated capillary radius values.

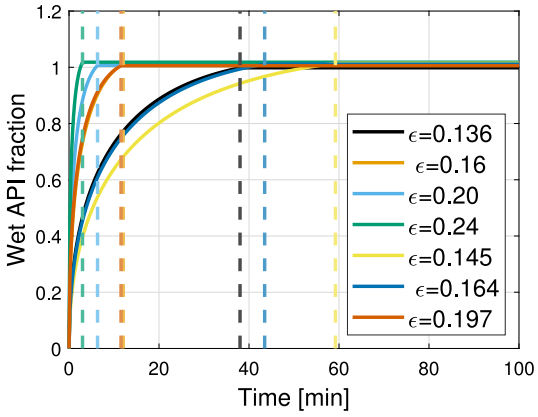

Fig. 12. Tablet wetting kinetics, wet API fraction as a function of time. The vertical dotted lines indicate the time scale when the tablet is fully wet, or the wet API fraction is one.

automatically making r_e, k_{API}, and CSD the parameters that dominate tablet dissolution profile.

6. Concluding remarks

We have proposed a two-stage ROM of pharmaceutical tablet dissolution that is comprised of (i) a *mechanistic API dissolution function* derived from a population balance model (PBM) using a high-resolution finite volume algorithm (HR-FVM) for a given API crystal size distribution and dissolution rate coefficient, and (ii) a *tablet wetting function* that estimates the rate at which the API is exposed to the buffer solution for given formulation and dimensions of the tablet, contact angle and surface tension between the solid and liquid phases, liquid viscosity, and mean effective capillary radius of the porous microstructure. The tablet wetting function is obtained from the mechanistic understanding of water penetration inside a porous tablet, and it was validated using a time-resolved micro-CT test. The model parameters of the API dissolution function, here being the dissolution rate coefficient, are readily available from dissolution tests of API crystals. In turn, the two-stage model is mechanistic in nature and one-way coupled by means of convolution in time to capture the start time of the API dissolution process as water uptake, swelling, and disintegration take place. A notable feature of the ROM is that it is computationally efficient and suitable for realizing RTRT and QbC strategies if coupled with a suit of tableting ROMs to estimate tablet content uniformity, weight, dimensions, and porosity. We have also developed a parameter estimation method aimed at maximizing the f_2 similarity factor between model predictions and experimental dissolution data. Finally, we have showcased the versatility and the effectiveness of the mechanistic API dissolution model and the two-stage tablet dissolution ROM to predict the dissolution profile of various pharmaceutical formulations and its connection with CMAs, CPPs, and other CQAs, namely initial API crystal size distribution, and porosity, composition, and dimensions of the tablet. Specifically, we have fabricated and formulated solid oral tablets containing acetaminophen and lomustine using different API content and size distributions, characterized their dissolution behavior, and estimated capillary radius as a function of tablet porosity. In all of the cases examined in this study, the predictions of the proposed models closely align with the experimental data, showcasing the ability of the two-stage ROM to automatically identify the physical mechanisms that control the dissolution process, i.e., identifying whether API dissolution is strongly coupled and mediated by the wetting process or rather weakly mediated. For formulations that exhibit disintegration upon water uptake, tablet wetting functions endowed with disintegration events that, in turn, would speed up the API wetting process are desirable if beyond the scope of this paper.

CRediT authorship contribution statement

Shumaiya Ferdoush: Writing – review & editing, Writing – original draft, Visualization, Validation, Software, Methodology, Investigation, Formal analysis, Data curation, Conceptualization. **Marcial Gonzalez:** Writing – review & editing, Supervision, Resources, Project administration, Methodology, Funding acquisition, Conceptualization.

Declaration of competing interest

The authors declare that they have no known competing financial interests or personal relationships that could have appeared to influence the work reported in this paper.

Data availability

Data will be made available on request.

Acknowledgments

The authors acknowledge with gratitude the support received from the U.S. Food and Drug Administration grant numbers 1U01FD006738-01, 5U01FD006738-02, and 5U01FD006738-03 entitled “Risk-based process synthesis and Industry 4.0 framework for pharmaceutical manufacturing processes”, and the National Science Foundation grant number 2140452 entitled “Right First Time Manufacturing of Pharmaceuticals (RIFTMaP)”. The authors express their gratitude to Gamlen Instruments (London, UK) for providing the Gamlen D Series benchtop compaction simulator. The authors also extend their appreciation to Professor Zoltan Nagy and Dr. Jaron Mackey at Purdue University for producing the lomustine crystals that are utilized in the experiments outlined in this study. The authors would like to express their sincere appreciation to Professor James Litster at The University of Sheffield for generously dedicating his time and expertise to review this manuscript. His thoughtful feedback and constructive suggestions significantly contributed to the improvement of this paper. Finally, SF acknowledges the support provided by the School of Mechanical Engineering at Purdue University through the Bilsland Fellowship.

Appendix

Acetaminophen and lomustine tablet’s experimental data of weight, API mass, API concentration, and dimensions are listed in Tables 7 and 8. All data points are an average of three sets of data.

Table 7
Acetaminophen tablet's (three different formulations with varying APAP concentrations) weight, API mass, API concentration and dimension data.

APAP concentration	17% APAP				RSD (%)	9% APAP				RSD (%)	2% APAP				RSD (%)
In-die relative density	0.95	0.9	0.85	0.8		0.95	0.9	0.85	0.8		0.95	0.9	0.85	0.8	
Tablet weight, W (mg)	153.66	152.57	153.19	152.74	0.321	153.40	151.93	153.13	153.73	0.51	152.53	152.38	152.19	153.10	0.26
Mass of API, m_{API} (mg)	26.59	26.30	24.59	26.79	3.859	13.52	13.22	13.14	12.35	3.82	3.50	3.20	3.06	2.97	7.30
API conc., x_{API} (w/w)	0.17	0.17	0.16	0.18	3.919	0.09	0.09	0.09	0.08	4.05	0.02	0.02	0.02	0.02	7.38
Tablet radius, R_{tab} (mm)	3.02	3.03	3.03	3.04	0.184	3.03	3.03	3.03	3.04	0.09	3.03	3.03	3.04	3.04	0.10
Tablet height, H_{tab} (mm)	5.25	5.56	5.77	6.13	6.498	5.29	5.39	5.86	6.06	6.55	5.28	5.48	5.73	6.08	6.06

Table 8
Lomustine tablet's weight, API mass, API concentration and dimension data.

CSD	0–180 μm				RSD (%)	125–250 μm			RSD (%)
In-die relative density	0.95	0.90	0.85	0.80		0.95	0.90	0.85	
Tablet weight, W (mg)	114.37	114.17	114.13	113.97	0.14	114.30	114.23	114.50	0.12
Mass of API, m_{API} (mg)	5.54	4.19	4.33	4.40	13.44	5.22	5.09	5.13	1.28
API conc, x_{API} (w/w)	0.05	0.04	0.04	0.04	13.31	0.05	0.04	0.04	1.28
Tablet radius, R_{tab} (mm)	3.03	3.03	3.02	3.02	0.19	3.03	3.02	3.01	0.33
Tablet height, H_{tab} (mm)	3.02	3.10	3.27	3.45	5.95	3.05	3.12	3.28	3.74

References

Bachawala, S., Gonzalez, M., 2022. Development of mechanistic reduced order models (ROMs) for glidant and lubricant effects in continuous manufacturing of pharmaceutical solid-dosage forms. In: Computer Aided Chemical Engineering. Vol. 51, Elsevier, pp. 1129–1134.

Bachawala, S., Nasilowski, D., Gonzalez, M., 2024. Semi-mechanistic reduced order model of pharmaceutical tablet compaction for continuous manufacturing: Lubricant and glidant effects. in preparation, Unpublished results.

Bhalekar, M.R., Desale, S.S., Madgulkar, A.R., 2010. Synthesis of MCC–PEG conjugate and its evaluation as a superdisintegrant. AAPS PharmSciTech 11 (3), 1171–1178.

Borhan, A., Rungta, K., 1993. An experimental study of the radial penetration of liquids in thin porous substrates. J. Colloid Interface Sci. 158 (2), 403–411.

Callegari, G., Awad, T., Wang, Y., Pawar, P., Pastrana, I., Drazer, G., Muzzio, F.J., Cuitino, A., 2013. The effect of blend shearing and compression on dissolution dynamics for immediate release tablets. In: AIChE Annual Meeting.

Costa, P., Lobo, J.M.S., 2001. Modeling and comparison of dissolution profiles. European journal of pharmaceutical sciences 13 (2), 123–133.

Costa, C.B.B., Maciel, M.R.W., Maciel Filho, R., 2007. Considerations on the crystallization modeling: Population balance solution. Comput. Chem. Eng. 31 (3), 206–218.

Danino, D., Marmur, A., 1994. Radial capillary penetration into paper: limited and unlimited liquid reservoirs. J. Colloid Interface Sci. 166 (1), 245–250.

Depalo, A., Santomaso, A.C., 2013. Wetting dynamics and contact angles of powders studied through capillary rise experiments. Colloids Surf. A 436, 371–379.

FDA, 2004. Guidance for industry: PAT-A framework for innovative pharmaceutical development, manufacturing and quality assurance. http://www.fda.gov/cder/guidance/published.hml.

FDA, 2012. Guidance for Industry: Q11 Development and Manufacture of Drug Substances. US Department of Health and Human Services.

FDA, CDER, 1997. Guidance for industry: Dissolution testing of immediate release solid oral dosage forms.

FDA, CDER, 2006. Guidance for industry: Q8 pharmaceutical development.

Ferdoush, S., Gonzalez, M., 2023. Semi-mechanistic reduced order model of pharmaceutical tablet dissolution for enabling Industry 4.0 manufacturing systems. Int. J. Pharm. 631, 122502.

Ferdoush, S., Kzam, S.B., Martins, P.H., Dewanckele, J., Gonzalez, M., 2023. Fast time-resolved micro-CT imaging of pharmaceutical tablets: Insights into water uptake and disintegration. Int. J. Pharm. 648, 123565.

Ghazi, N., Liu, Z., Bhatt, C., Kiang, S., Cuitino, A., 2019. Investigating the effect of APAP crystals on tablet behavior manufactured by direct compression. Aaps Pharmscitech 20, 1–14.

Gunawan, R., Fusman, I., Braatz, R.D., 2004. High resolution algorithms for multidimensional population balance equations. AIChE J. 50 (11), 2738–2749.

Hamraoui, A., Nylander, T., 2002. Analytical approach for the Lucas–Washburn equation. J. Colloid Interface Sci. 250 (2), 415–421.

Hayashi, T., Ogura, T., Takagishi, Y., 1995. New evaluation method for in vitro/in vivo correlation of enteric-coated multiple unit dosage forms. Pharmaceutical research 12, 1333–1337.

Huang, Y.-S., Sheriff, M.Z., Bachawala, S., Gonzalez, M., Nagy, Z.K., Reklaitis, G.V., 2021. Evaluation of a combined MHE-NMPC approach to handle plant-model mismatch in a rotary tablet press. Processes 9 (9), 1612.

Hyväluoma, J., Raiskinmäki, P., Jäsberg, A., Koponen, A., Kataja, M., Timonen, J., 2006. Simulation of liquid penetration in paper. Phys. Rev. E 73 (3), 036705.

Kristó, K., Bajdik, J., Kleinebudde, P., Pintye-Hódi, K., 2010. Effect of lubricant on spreading of coating liquid on surface of tablets containing pancreatin. Pharm. Dev. Technol. 15 (4), 354–359.

Lawrence, X.Y., Amidon, G., Khan, M.A., Hoag, S.W., Polli, J., Raju, G., Woodcock, J., 2014. Understanding pharmaceutical quality by design. AAPS J. 16 (4), 771–783.

LeBlanc, S., Fogler, H.S., 1987. Population balance modeling of the dissolution of polydisperse solids: rate limiting regimes. AIChE J. 33 (1), 54–63.

Lima, F.A.R.D., Barreto Correa, G., de Moraes, M.G.F., Segtovich, I.S.V., Barreto Junior, A.G., Pinto, J.C., 2023. Statistical analyses of a population balance model of a batch crystallization process. Cryst. Growth Des. 24 (1), 308–324.

Litster, J., 2016. Design and Processing of Particulate Products. Cambridge University Press.

2024. Lomustine. Chemsrc. (n.d.) (n.d.). https://www.chemsrc.com/en/cas/13010-47-4_894596.html. (Accessed 06 April 2024).

Lu, A.T., Frisella, M.E., Johnson, K.C., 1993. Dissolution modeling: factors affecting the dissolution rates of polydisperse powders. Pharm. Res. 10, 1308–1314.

Mackey, J., Mufti, A., Lee, S.-L., Abdi, M., Feng, X., Wood, E., Thompson, D.H., Nagy, Z., 2020. Process design and development of a small scale hybrid manufacturing system for the cancer drug lomustine. In: 2020 Virtual AIChE Annual Meeting. AIChE.

Mangin, D., Garcia, E., Gerard, S., Hoff, C., Klein, J., Veesler, S., 2006. Modeling of the dissolution of a pharmaceutical compound. J. Cryst. Growth 286 (1), 121–125.

Markl, D., Yassin, S., Wilson, D.I., Goodwin, D.J., Anderson, A., Zeitler, J.A., 2017. Mathematical modelling of liquid transport in swelling pharmaceutical immediate release tablets. Int. J. Pharm. 526 (1–2), 1–10.

Marmur, A., 1988. The radial capillary. J. Colloid Interface Sci. 124 (1), 301–308.

2020. MATLAB Version 9.8.0.1380330 (R2020a) [Computer software manual]. Natick, Massachusetts.

Nagy, Z., Aamir, E., Rielly, C., 2011. Internal fines removal using population balance model based control of crystal size distribution under dissolution, growth and nucleation mechanisms. Cryst. Growth Des. 11 (6), 2205–2219.

Nagy, B., Szilágyi, B., Domokos, A., Vészi, B., Tacsi, K., Rapi, Z., Pataki, H., Marosi, G., Nagy, Z.K., Nagy, Z.K., 2021. Dynamic flowsheet model development and digital design of continuous pharmaceutical manufacturing with dissolution modeling of the final product. Chem. Eng. J. 419, 129947.

Parvaresh, R., Ferdoush, S., Kshirsagar, S., Gonzalez, M., Nagy, Z.K., 2024. Integrated continuous crystallization—Spherical agglomeration (CCSA) process for the intensified manufacturing of atorvastatin calcium. Cryst. Growth Des..

Peppas, N.A., Narasimhan, B., 2014. Mathematical models in drug delivery: How modeling has shaped the way we design new drug delivery systems. J. Control. Release 190, 75–81.

Puel, F., Févotte, G., Klein, J., 2003. Simulation and analysis of industrial crystallization processes through multidimensional population balance equations. Part 1: a resolution algorithm based on the method of classes. Chem. Eng. Sci. 58 (16), 3715–3727.

Ranodolph, A., 2012. Theory of Particulate Processes: Analysis and Techniques of Continuous Crystallization. Elsevier.

Rawlings, J.B., Miller, S.M., Witkowski, W.R., 1993. Model identification and control of solution crystallization processes: a review. Ind. Eng. Chem. Res. 32 (7), 1275–1296.

Rawlings, J.B., Witkowski, W.R., Eaton, J.W., 1992. Modelling and control of crystallizers. Powder Technol. 69 (1), 3–9.

Razavi, S.M., Gonzalez, M., Cuitiño, A.M., 2018. Quantification of lubrication and particle size distribution effects on tensile strength and stiffness of tablets. Powder Technol. 336, 360–374.

Rowe, R.C., Sheskey, P., Quinn, M., 2009. Handbook of Pharmaceutical Excipients. Libros Digitales-Pharmaceutical Press.

Schott, H., 1992a. Kinetics of swelling of polymers and their gels. J. Pharm. Sci. 81 (5), 467–470.

Schott, H., 1992b. Swelling kinetics of polymers. J. Macromol. Sci. B: Phys. 31 (1), 1–9.
Steele, D.F., Moreton, R.C., Staniforth, J.N., Young, P.M., Tobyn, M.J., Edge, S., 2008. Surface energy of microcrystalline cellulose determined by capillary intrusion and inverse gas chromatography. AAPS J. 10, 494–503.
Su, Q., Bommireddy, Y., Gonzalez, M., Reklaitis, G.V., Nagy, Z.K., 2018. Variation and risk analysis in tablet press control for continuous manufacturing of solid dosage via direct compaction. In: Computer Aided Chemical Engineering. Vol. 44, Elsevier, pp. 679–684.
Su, Q., Ganesh, S., Moreno, M., Bommireddy, Y., Gonzalez, M., Reklaitis, G.V., Nagy, Z.K., 2019. A perspective on quality-by-control (QbC) in pharmaceutical continuous manufacturing. Comput. Chem. Eng. 125, 216–231.
Su, Q., Hermant, P., Casati, F., Halkude, B., Wu, W., Ramnath, A., Dubey, A., Born, S., Takizawa, B., Mascia, S., 2023. Model predictive in vitro dissolution testing in pharmaceutical continuous manufacturing: An equivalence study. AIChE J. 69 (9), e18124.
Sun, C., 2004. A novel method for deriving true density of pharmaceutical solids including hydrates and water-containing powders. J. Pharm. Sci. 93 (3), 646–653.
USP, 2011. 711 Dissolution.
Van Leer, B., 1974. Towards the ultimate conservative difference scheme. II. Monotonicity and conservation combined in a second-order scheme. J. Comput. Phys. 14 (4), 361–370.
Washburn, E.W., 1921. The dynamics of capillary flow. Phys. Rev. 17 (3), 273.
Wilson, D., Wren, S., Reynolds, G., 2012. Linking dissolution to disintegration in immediate release tablets using image analysis and a population balance modelling approach. Pharm. Res. 29, 198–208.
Witono, J.R., Noordergraaf, I., Heeres, H., Janssen, L., 2014. Water absorption, retention and the swelling characteristics of cassava starch grafted with polyacrylic acid. Carbohydr. Polym. 103, 325–332.
Wu, H., Lyon, R.C., Khan, M.A., Voytilla, R.J., Drennen III, J.K., 2015. Integration of near-infrared spectroscopy and mechanistic modeling for predicting film-coating and dissolution of modified release tablets. Ind. Eng. Chem. Res. 54 (22), 6012–6023.
Zaborenko, N., Shi, Z., Corredor, C.C., Smith-Goettler, B.M., Zhang, L., Hermans, A., Neu, C.M., Alam, M.A., Cohen, M.J., Lu, X., et al., 2019. First-principles and empirical approaches to predicting in vitro dissolution for pharmaceutical formulation and process development and for product release testing. AAPS J. 21, 1–20.